

Texture and Grain Boundary Network Evolution of Laser Powder Bed Fusion Processed Pure Ni During Post-printing Annealing



HOSSEIN BELADI, HAMIDREZA TORBATI-SARRAF, GREGORY S. ROHRER, BEHRANG POORGANJI, and SEYED ALIREZA TORBATI-SARRAF

Commercially pure Ni was additively manufactured using laser powder bed fusion. The printed specimens were then subjected to annealing treatments in a range of 700 °C to 1200 °C to investigate the evolution of the microstructure using electron backscatter diffraction mapping and a five-parameter analysis of the grain boundary character distribution. The post-printing annealing treatment resulted in microstructural changes in respect to grain shape and size, the grain boundary character distribution and the overall texture. However, the extent of these changes strongly depended on the annealing temperature. The grain structure and overall texture changed only modestly when annealed below 900 °C. The grains grew by about 10 pct and this led to a small (≈ 15 pct) increase in the areas of boundaries with low energy (111) planes at the expense of higher energy grain boundary planes with the (001) orientation. Static recrystallization was the dominant microstructure evolution mechanism at annealing temperatures greater than 1000 °C, where new equiaxed grains replaced the initial printed microstructure, enhancing the relative areas of low energy grain boundaries (*i.e.*, $\sum 3$ and $\sum 9$) by a factor of more than five. This change increased the population of boundaries with the low energy (111) plane by a factor of five and decreased the strength of the texture by more than 50 pct through twinning. The resultant microstructure is expected to ultimately improve the material properties, where the increase in the relative areas of $\sum 3$ boundaries would enhance the corrosion resistance and fracture toughness of material, and the texture weakening diminishes the anisotropy in mechanical behaviour.

<https://doi.org/10.1007/s11661-022-06782-3>
© The Author(s) 2022, corrected publication 2022

I. INTRODUCTION

ADDITIVE manufacturing (AM) is a promising technology that transforms customization and flexibility in metal processing, offering an attractive route to manufacture critical components. Laser powder bed fusion (L-PBF) is the most common fusion-based metal additive manufacturing (AM) technique, where a

layer-by-layer metal deposition method is employed through melting the powders to consolidate a near shape parts. During this process, a local melt pool is formed when a laser irradiates a powder bed, then solidifies at a cooling rate of up to 10^7 °C/s.^[1,2] The directional thermal gradients inherent in this process cause microstructural complexities such as anisotropic texture and the formation of dislocation networks within the grain interiors.^[3-6]

Due to good metallurgical, mechanical, and high oxidation resistance properties of Ni-based superalloys, L-PBF processing of these alloys is technologically viable in the energy, transportation, and semiconductor industries. The microstructure of L-PBF processed Ni-based alloys with the FCC (Face Centered Cubic) crystal structure typically displays elongated/coarse grains along the build direction, promoting specific crystallographic texture (*e.g.*, $\langle 100 \rangle$ and/or $\langle 110 \rangle$). This anisotropic texture mainly originates from preferential solidification of FCC crystals along the $\langle 100 \rangle$ axis, which aligns with the heat flux direction.^[7-9] In some applications such as high temperature turbine blades,

HOSSEIN BELADI is with the Institute for Frontier Materials, Deakin University, Geelong, VIC 3216, Australia. Contact e-mail: hossein.beladi@deakin.edu.au HAMIDREZA TORBATI-SARRAF is with the School of Materials Engineering, Purdue University, West Lafayette, IN 47907. GREGORY S. ROHRER is with the Department of Materials Science and Engineering, Carnegie Mellon University, Pittsburgh, PA 15213-3890. BEHRANG POORGANJI is with the Department of MIME, The University of Toledo, Toledo, OH 43606. SEYED ALIREZA TORBATI-SARRAF is with the Departments of Aerospace & Mechanical Engineering and Materials Science, University of Southern California, Los Angeles, CA 90089. Manuscript submitted May 2, 2022; accepted July 27, 2022. Article published online August 14, 2022

Table I. The EBSD Conditions for Different Post-print Annealing Treatments

Condition	Step Size (μm)	Area	Number of Boundary Segments
As-Built	1	$1200 \mu\text{m} \times 600 \mu\text{m} \times 7$	$\sim 50,000$
700 °C	1	$1200 \mu\text{m} \times 600 \mu\text{m} \times 7$	$\sim 50,000$
900 °C	1	$1200 \mu\text{m} \times 600 \mu\text{m} \times 8$	$\sim 60,000$
1000 °C	1	$1200 \mu\text{m} \times 600 \mu\text{m} \times 10$	$\sim 57,000$
1200 °C	1	$1200 \mu\text{m} \times 600 \mu\text{m} \times 16$	$\sim 50,000$

the elongated grains with strong crystallographic texture would be beneficial to restrict the grain boundary sliding (*i.e.*, creep phenomenon).^[10] However, the introduction of strong texture leads to an anisotropy in the material performance, including yield strength, corrosion, and electrochemical behaviour.^[9,11–16] This also influences the grain boundary network, for example, restricting the formation of coincidence site lattice (CSL) boundaries (such as annealing twins) in FCC materials,^[6,17,18] which control the material toughness^[19] and corrosion behaviour.^[20]

The grain morphology and size can be altered by changing the laser scanning strategy, which appears to improve the material performance.^[21–23] However, the material, to some degree, maintains a specific crystallographic texture due to the nature of rapid solidification, where the grains directionally grow preferentially along the greatest heat flux direction upon the solidification.^[24] As a result, process modification does not fully eliminate the anisotropy in material properties and ultimately modifies the grain boundary network due to the presence of a relatively strong texture. Therefore, a new approach is required to alter the additively manufactured microstructure in terms of grain structure and weaken the overall crystallographic texture. Post-process annealing has been studied extensively for its effect on texture weakening and the improvement isotropic properties after severe plastic deformation.^[25,26]

The presence of a high dislocation density in AM materials due to the rapid solidification process can be utilized as a driving force to activate recovery and/or recrystallization restoration processes, which may take place during post-printing annealing. This may ultimately lead to the modification of the grain structure, crystallographic texture, and grain boundary network. More recently, post-built annealing treatment were performed on AM metals to improve the material performance through the modification in microstructure and texture.^[6,27,28] However, they largely worked on recrystallization in highly alloyed materials (*e.g.*, AISI 316L and IN718 alloys), where the presence of a second phase and composition inhomogeneity, to large extent, retards the grain boundary mobility (*i.e.*, kinetics of recrystallization) and subsequently affects the extent of microstructure and texture evolution.^[6,27,28] In addition, the prior studies provide limited information on the effect of post-built annealing treatment on the evolution of grain boundary network.

Therefore, this study aimed to assess the grain structure, texture and grain boundary network evolution of a L-PBF processed commercially pure Ni part by means of annealing in a range of 700 °C to 1200 °C. To isolate the contribution of texture and eliminate the effect of alloying elements on the stacking fault energy and the formation of phases and/or cellular structures, commercially pure Ni was considered as a baseline FCC crystal structure material for this study. Orientation mapping by electron backscatter diffraction and a five-parameter analysis of the grain boundary character distribution were employed to reveal the mechanism/s controlling microstructure evolution during the post-printing annealing treatment in the temperature range between 700 °C and 1200 °C.

II. EXPERIMENTAL PROCEDURE

Atomized powder of commercially pure Ni with a composition of Ni–0.16Si–0.20–0.17Fe (wt pct) was used to produce cube samples with dimensions of $1 \times 1 \times 1 \text{ cm}^3$ by means of laser powder bed fusion additive manufacturing using an EOS M400-1 with 40 μm layer thickness. The laser line orientation was iteratively rotated by 67 deg after printing each layer.

To study the effect of post-printing annealing treatment on the microstructure evolution, the as-printed cubes were heat treated using a tube furnace under Ar gas at a temperature range of 700 °C to 1200 °C for 2 hours followed by air cooling to ambient. The microstructure was characterised by means of a scanning electron microscope equipped with an electron backscatter diffraction (EBSD) detector. Specimens for EBSD characterisation were prepared through a standard polishing routine, consisting of grinding by 600 and 1200 grit sandpapers, followed by polishing by means of 9, 3 and 1 μm suspensions in successive steps. Then, they were further polished using a colloidal silica slurry solution. FEI Quanta 3D FEG FIB-SEM microscope was employed to acquire EBSD maps using 20 kV voltage and 8 nA current with a step size of 1 μm .

Multiple EBSD maps were acquired, covering a large area ranging from ~ 5 to $\sim 11.5 \text{ mm}^2$ depending on the microstructure characteristics (Table I). The EBSD maps were conducted parallel and perpendicular to the build direction, to minimize texture bias in the grain

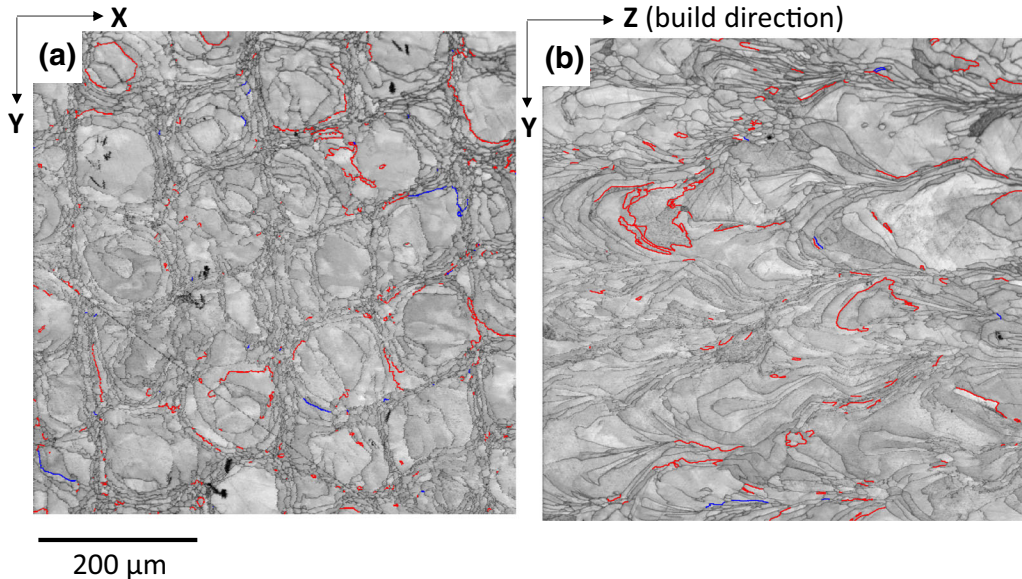


Fig. 1—The band contrast EBSD images of as-printed microstructure of commercially pure Ni at different cross sections in respect to build direction (Z). (a) The plane perpendicular to the build direction (*i.e.*, X - Y) and (b) the plane parallel to the build direction (*i.e.*, Y - Z). Red and blue lines are $\Sigma 3$ and $\Sigma 9$ boundaries, respectively (Color figure online).

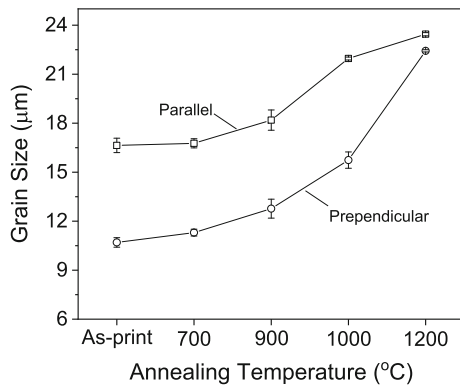


Fig. 2—The grain size at different cross-sections in respect to the build direction (*i.e.*, perpendicular and parallel to the build direction) at different annealing treatment temperatures.

boundary characterisation. TSL-OIM™ software was employed to post-process the data, using a series of cleaning procedures, namely grain dilation, a single average orientation per grain assignment and boundary reconstruction. The latter was utilized to extract the boundary line segments, which were interpreted stereologically to measure the distribution of grain boundary plane orientations, known as five-parameter grain boundary analysis.^[29] At least 50,000 grain boundary line segments were collected for each condition (Table I), which is the minimum requirement to reliably measure the grain boundary plane character distribution for materials with cubic crystal structure.^[29] Based on the Brandon criterion, the angular tolerance of 8.66 and 5 deg from the corresponding ideal lattice misorientation was used to define $\Sigma 3$ and $\Sigma 9$ boundaries,

respectively.^[30] In the current study, a minimum misorientation angle of 15 deg was considered as a grain boundary to define a grain. The grain size was determined by means of the equivalent circular diameter approach. For each post-built annealing treatment, the grain size measurement was performed for multiple EBSD maps acquired at different cross-sections with respect to the build direction to remove the texture bias. The statistical error was computed using the standard error = $\frac{S}{\sqrt{N}}$, where S and N are standard deviation and number of measurements, respectively.

III. RESULTS AND DISCUSSION

The as-printed microstructure revealed distinct grain morphologies depending on orientation of the surface with respect to the build direction. The surface perpendicular to the build direction (XY) displayed a checkerboard pattern as a result of cross-hatching of the laser scans (Figure 1(a)).^[24,31] A semi-columnar structure appeared in the surface along the build direction (*i.e.*, YZ , Figure 1(b)), attributed to the directional growth of grains preferably along the steepest heat flux direction during the cyclic melting and solidification.^[24] Because of the anisotropic grain shape, the mean grain size depended on the orientation of the observation plane and was $10.7 \pm 0.3 \mu\text{m}$ and $16.6 \pm 0.4 \mu\text{m}$ at surfaces perpendicular and parallel to the build direction, respectively (Figure 2).

During the solidification, dendrites preferably adopt an orientation near to the heat flux direction, having their growth direction along the axis of a pyramid consisting of four $\{111\}$ close packed planes for materials with face-centered cubic (FCC) crystal structure

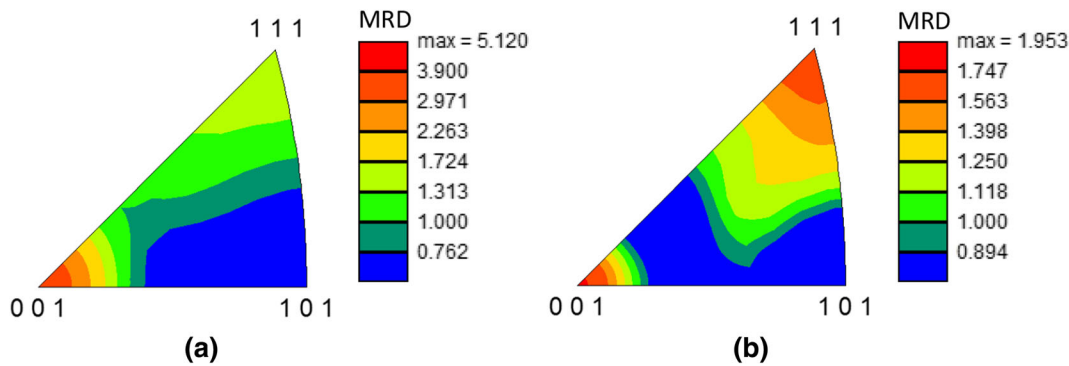


Fig. 3—Inverse pole figure along the normal direction of as-printed (a) and annealed at a temperature of 1200 °C (b) conditions. MRD represents multiples of a random distribution.

(*i.e.*, Ni).^[8] The intersection of {111} pyramid planes leads to $\langle 100 \rangle$ axis, which is the ideal solidification direction projected into the melt front interface.^[32,33] As the laser path iteratively rotates by 67 deg after each printing layer, $\langle 100 \rangle$ axis maintains a constant angle of ~ 45 deg with the build direction to reduce the deviation angle between the primary dendrite growth direction and the maximum heat flow direction in subsequent deposited/printed layers.^[33] This leads to the columnar grains not being perfectly aligned with the build direction (Figure 1(b)), and most importantly the formation of a relatively strong texture about the (001) orientation with a strength of ~ 5.1 multiples of a random distribution (Figure 3(a)). The misorientation angle distribution of as-printed microstructure deviated from the random distribution, displaying two moderate peaks at ~ 8 and ~ 45 deg (Figure 4(a)). There are few CSL boundaries (*i.e.*, $\Sigma 3$ and $\Sigma 9$, Figure 1) observed in the as-built microstructure, and they are largely isolated. In other words, $\Sigma 9$ boundaries are not connected to any $\Sigma 3$ boundaries in the section plane. This suggests that CSL boundaries (*i.e.*, $\Sigma 3$ and $\Sigma 9$) are not formed through multiple twinning, as seen in the conventional recrystallized microstructure, and their presence is coincidental.

The post-printing annealing heat treatment did not change the microstructure characteristics up to 900 °C (Figure 5). This was also reflected in the misorientation angle distribution, as they maintained their overall characteristics up to 900 °C. However, the mean grain size increased by about 10 pct with the annealing temperature up to 900 °C. This suggests that the annealing treatment most likely led to the recovery of dislocations and/or grain growth. Higher temperature annealing led to larger increases in the grain size (Figure 2). This was due to the appearance of new equiaxed grains, partially replacing the as-printed microstructure at 1000 °C (Figures 5(c) and (d)). This suggests the occurrence of static recrystallization due to the presence of high-dislocation density induced upon printing (rapid solidification) and appropriate annealing temperature regime. During the static recrystallization (SRX), the new grains largely nucleate on the region/s with high stored energy/dislocation density (*i.e.*, grain boundaries) and grow into adjacent grain/s. It appeared

SRX nucleation takes place inhomogeneously within the as-built microstructure (Figures 5(c) and (d)), preferentially on laser beam tracks due to higher local stored energy (dislocation density) imposed by the L-PBE process, as reported elsewhere.^[6] The SRX grains largely have equiaxed morphology, free of dislocations and promote the formation of low energy CSL boundaries (*i.e.*, $\Sigma 3$ and $\Sigma 9$) through multiple twinning (Figures 5(c) to (f)). Therefore, the partial recrystallization of the microstructure at 1000 °C resulted in a significant change in the misorientation angle distribution, revealing a relatively strong peak at ~ 60 deg and a small peak at ~ 39 deg (Figure 4(d)). The corresponding misorientation axes were clustered around the $\langle 111 \rangle$ and $\langle 101 \rangle$ directions in the standard stereographic triangle for boundaries with misorientation angles of 60 and 39 deg, respectively. This suggests the formation of first order annealing twin $\Sigma 3$ boundaries characterised by a 60 deg/ $\langle 111 \rangle$ lattice misorientation, which largely appeared within newly formed/recrystallized equiaxed grains (Figures 5(c) and (d)). The second most populated boundaries had 39 deg/ $\langle 101 \rangle$ lattice misorientation, representing $\Sigma 9$ boundaries. This boundary formed mostly from the impingement of two $\Sigma 3$ boundaries; this is known as twin multiplication.^[34] Therefore, their population is much lower than $\Sigma 3$ boundaries.

With an increase in the post-printing heat annealing temperature to 1200 °C, the microstructure was fully recrystallized to coarse equiaxed grains (Figures 5(e) and (f)), leading to further increases in the mean grain size (*i.e.*, $22.4 \pm 0.1 \mu\text{m}$ and $23.5 \pm 0.1 \mu\text{m}$ at the surfaces perpendicular and parallel to the build direction, respectively, Figure 2). The coarse recrystallized grains contained many annealing twin boundaries (Figures 5(e) and (f)). This resulted in the presence of a prominent peak at 60 deg and a relatively weak peak at 39 deg in the corresponding misorientation angle distribution (Figure 4(e)). In addition, the overall texture became relatively weak, with ~ 2 multiples of a random distribution, having two moderate peaks at (001) and (111) orientations (Figure 3(b)). The weakening of the texture is due to the occurrence of static recrystallization, which promotes the twinning multiplication process.

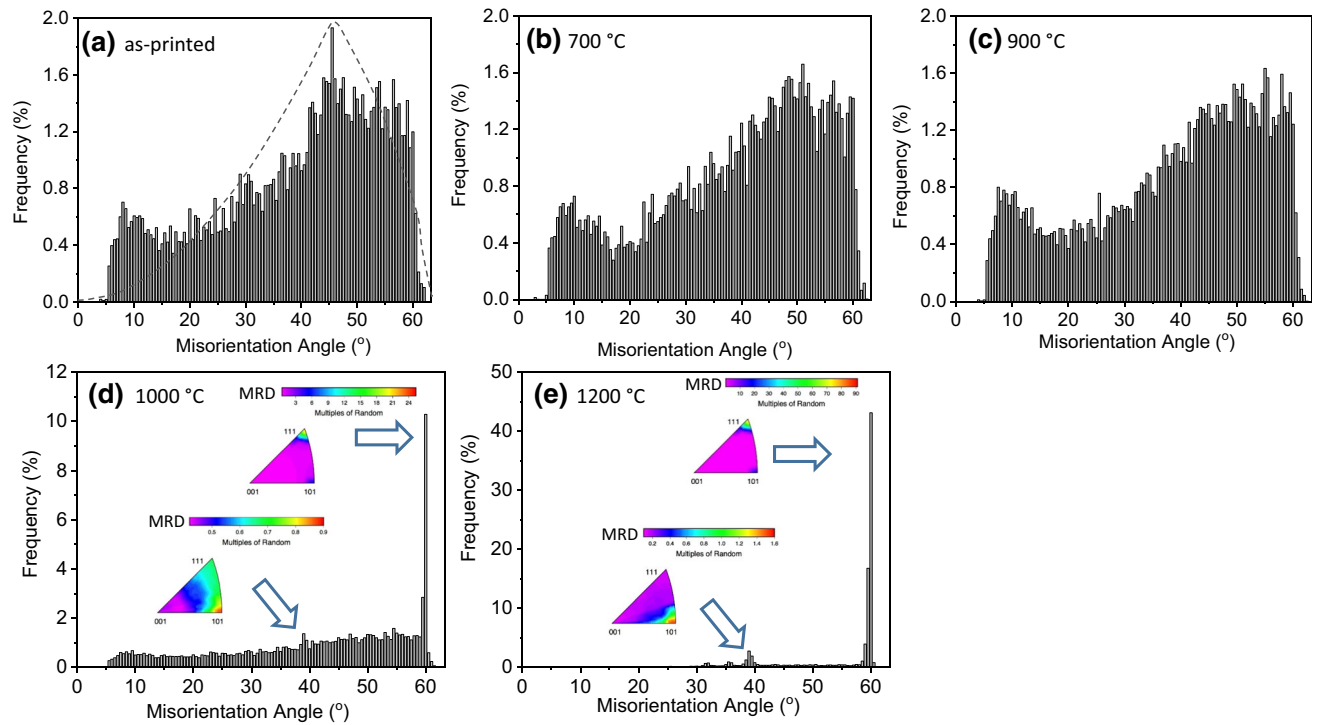


Fig. 4—Misorientation angle distribution for commercially pure Ni at different post-print annealing treatment temperatures. (a) as-printed, (b) 700 °C, (c) 900 °C, (d) 1000 °C and (e) 1200 °C. The dash line curve in (a) represents the random misorientation angle distribution. (d) and (e) include the distribution of axes at rotation angles of 60 and 39 deg in a standard stereographic triangle. MRD is multiples of a random distribution.

Grain Boundary Characteristics: The relative area distributions of grain boundary planes, independent of misorientation, were plotted in the crystal reference frame for different microstructures formed at different post-printing annealing treatment conditions. The distribution was computed using units of multiples of a random distribution (MRD), in which values more than 1 indicate that planes appeared more frequently than expected in a random distribution. The as-printed microstructure exhibited an anisotropy with a maximum at the position of (001) planes with 1.4 MRD. This suggests that the (001) plane population was ~ 40 pct greater than expected in a random distribution. The minima appeared at the (101) and (111) orientations where the intensity was ~ 0.9 MRD (Figure 6(a)). The distribution is significantly different from what is expected from pure Ni produced through conventional nucleation and growth mechanism (*e.g.*, recrystallization), where the (111) orientation appeared more frequently than others.^[35] Indeed, the current observation revealed that the (001) orientation with the highest energy had the largest relative area, while the plane with the smallest energy, (111), had a small relative area (Figure 6(f)). This discrepancy is associated with the low population of annealing twin boundaries in the microstructure produced through the current printing process (*i.e.*, 6.6 ± 0.1 pct, Figure 1) and the overall texture (Figure 3(a)). The former limits the presence of boundaries with (111) plane orientation with the minimum energy.^[35,36] The manifestation of a relatively strong $\langle 001 \rangle$ texture evolved during deposition

promotes the termination of planes with a (001) orientation. This is similar to other reports where cubic materials with strong $\{100\}$,^[18] $\{101\}$ ^[17] and $\{111\}$ ^[37] texture, stimulate the plane orientation of (100), (101) and (111), respectively.

The post-printing annealing treatment revealed a significant effect on the overall grain boundary plane distribution. The intensity of the (111) orientation progressively enhanced with an increase in the annealing temperature at the expense of (001) orientation (Figures 6(a) to (c)). The change was more pronounced at 1000 °C and above, where the highest intensity appeared at the (111) orientation and the minima became (001) orientation (Figures 6(d) and (e)). This suggests that the post-printing annealing treatment promotes the (111) low energy boundary at the expense of (001) high energy boundaries, which is linked to the microstructure evolution.

The grain size increased by about 10 pct when annealed at temperatures up to 900 °C (Figure 2). This is a result of grain boundary migration, which is driven by the presence of dislocations in the microstructure.^[3,4] This eventually advances boundaries with low energy interfaces through the annihilation of dislocations (recovery) at this temperature range, which is known as one of the grain boundary engineering mechanisms utilized for FCC materials.^[38] This was also reflected by a slight increase in the population of $\sum 3$ boundaries from 6.6 ± 0.1 pct at as-printed condition to 8.1 ± 0.1 pct at 900 °C annealing condition (Figure 7). The recovery eventually enhances the boundaries with a

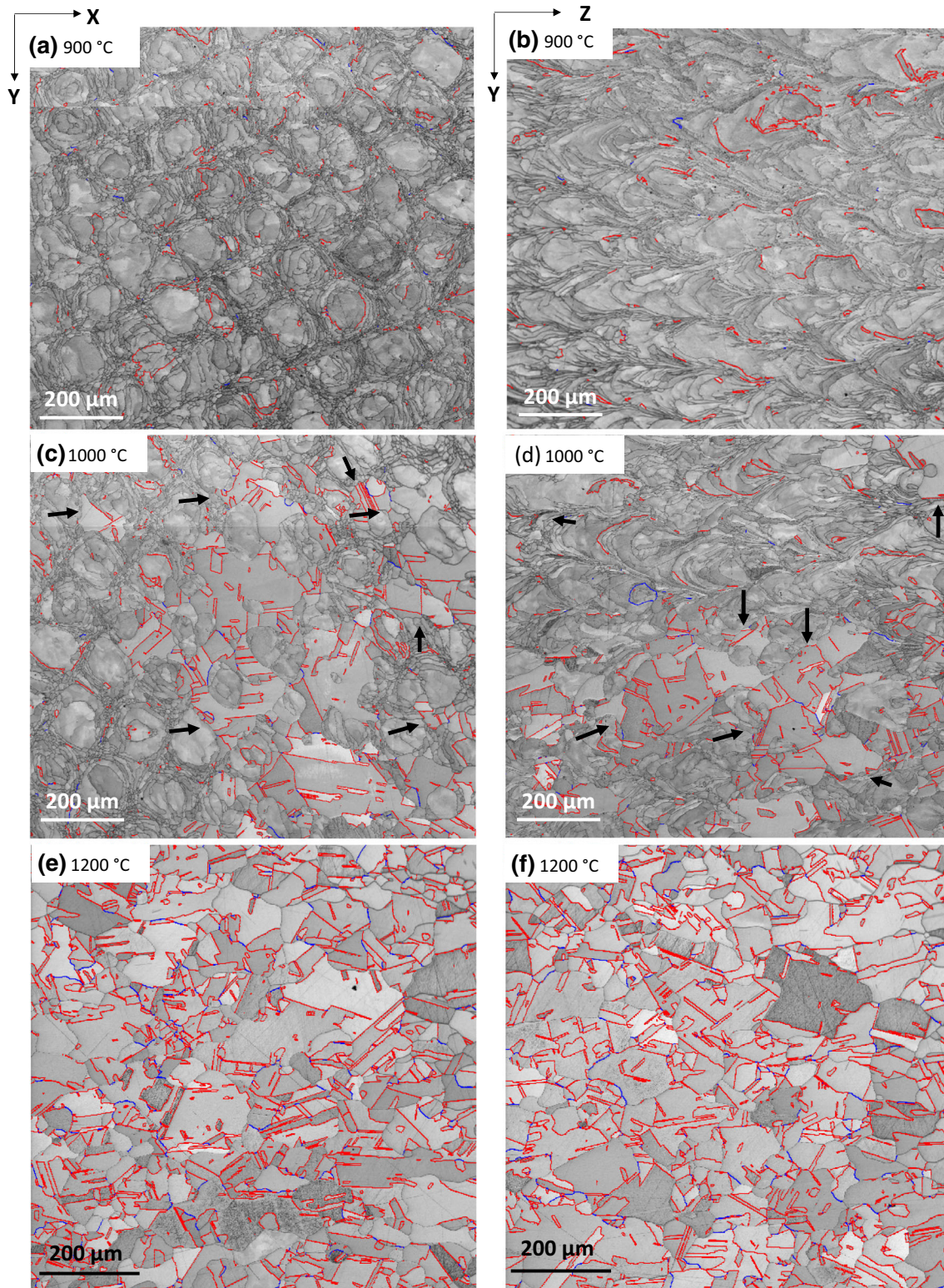


Fig. 5—The band contrast EBSD images of printed pure Ni at different annealing treatment temperatures at different cross sections in respect to the printing direction (Z). (a, b) 900 °C, (c, d) 1000 °C and (e, f) 1200 °C. X–Y and Y–Z represent the plane perpendicular and parallel to the printing direction, respectively. Red and blue lines are $\Sigma 3$ and $\Sigma 9$ boundaries, respectively. Arrows in c and d represent recrystallized grains (Color figure online).

low energy (111) plane orientations at the expense of the (001) plane orientation, having a relatively high energy (Figures 6(b) and (c)).

The (111) orientation became prominent after annealing at 1000 °C and above, presenting low energy boundaries (Figures 6(d) and (e)). The (111) peak

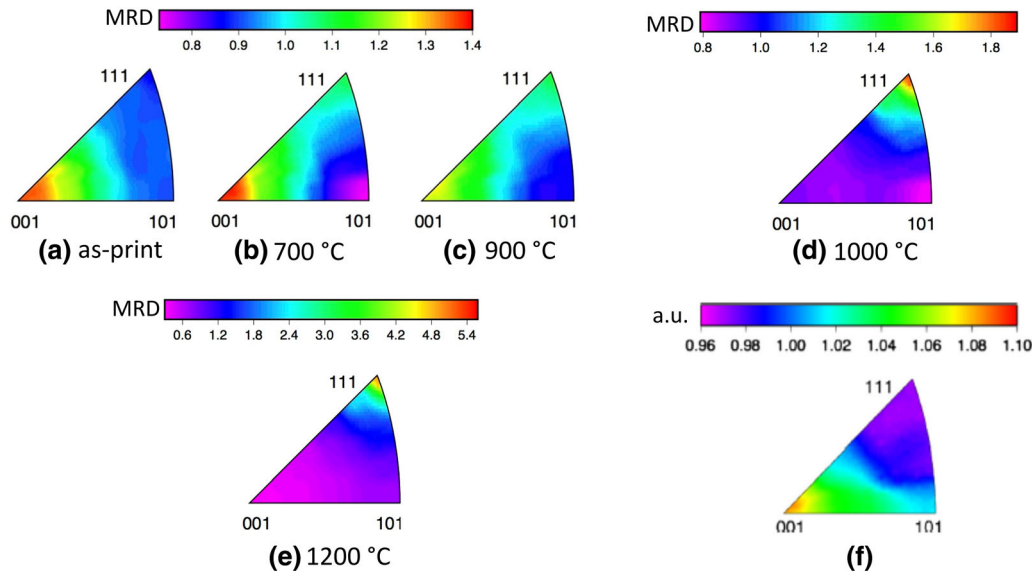


Fig. 6—(a through e) Grain boundary planes distribution, irrespective of misorientation, of commercially pure Ni subjected to different post-annealing treatments. (f) Grain boundary plane energy distribution, reprinted with permission from Ref. 35. MRD and a.u. represent multiples of a random distribution and arbitrary unit, respectively.

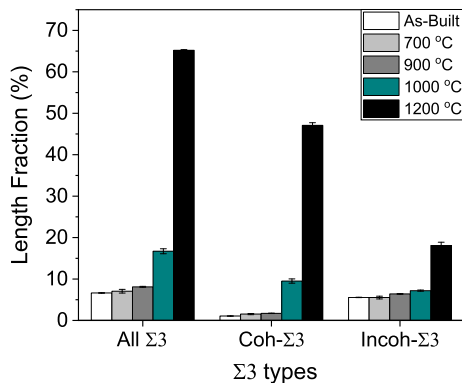


Fig. 7—Length fraction of $\Sigma 3$ boundaries with distinct characteristics at different annealing treatment temperatures. Coh- $\Sigma 3$ and Incoh- $\Sigma 3$ represent coherent and incoherent $\Sigma 3$ boundaries, respectively.

intensity grew from ~ 1.9 MRD in the partially recrystallized state at 1000 °C to ~ 5.5 MRD in the fully recrystallized state at 1200 °C (Figures 6(c) to (e)). Indeed, the initiation of static recrystallization is the prominent mechanism to promote low energy boundaries at high annealing temperature, as the equiaxed grains contain low energy $\Sigma 3$ CSL boundaries (Figures 5(c) to (f)).

The grain boundary plane distribution for $\Sigma 3$ boundaries (*i.e.*, 60 deg/ $\{111\}$ lattice misorientation) exhibited a prominent peak at the $\{111\}/\{111\}$ twist position for all microstructures, which is correlated to the minimum energy position in the distribution for FCC materials (Figure 8).^[35,36] The intensity of the (111) peak progressively increased with the annealing temperature and reflected as an increase in the number and relative areas of these boundaries. The (111) peak intensified significantly at 1000 °C and above annealing

treatment (Figures 8(d) and (e)), where static recrystallization appeared (Figures 5(c) to (f)). Static recrystallization increased the population of $\Sigma 3$ boundary to 16.7 ± 0.6 pct and 65.2 ± 0.2 pct for 1000 °C and 1200 °C, respectively (Figure 7).

The current AM process is known to create materials with a high dislocation density (*i.e.*, $\sim 10^{14} \text{ m}^{-2}$),^[5,6] appearing as dislocation cells. The dislocation substructure originates from thermal distortions during printing, primarily initiated by constraints surrounding the melt pool, very rapid cooling and subsequent alternating heating/cooling cycles.^[6] The introduction of the dislocation substructure may lead to the formation of steps on existing grain boundaries, which are prerequisites for the formation of annealing twins through growth accident model proposed by Mahajan *et al.*^[39] Among different models, the growth accident model provides more complete description of annealing twin formation, enabling the prediction of different twin morphologies. The model proposes that the annealing twins form on $\{111\}$ propagating steps that appear on moving grain boundaries. This “growth accident” leads to the generation of Shockley partials adjacent to the boundaries, which repel each other, producing a twin while gliding away from the boundary.^[39]

Interestingly, the population of $\Sigma 3$ boundaries formed through the current post-built annealing treatment (*i.e.*, ~ 65 pct, Figure 7) is relatively close to what was reported for commercially pure Ni subjected to a grain boundary engineering (GBE) process (*i.e.*, 63 pct $\Sigma 3$).^[40] This, however, contradicts work reported by others, where the population of $\Sigma 3$ boundaries was much lower in recrystallized as-built 316L stainless steel (~ 48 pct^[6]) compared with the one subjected to a GBE process (~ 79 pct^[41]). This difference can be, to some extent, related to the presence of nanoparticles in the as-built 316L stainless steel, which significantly retards

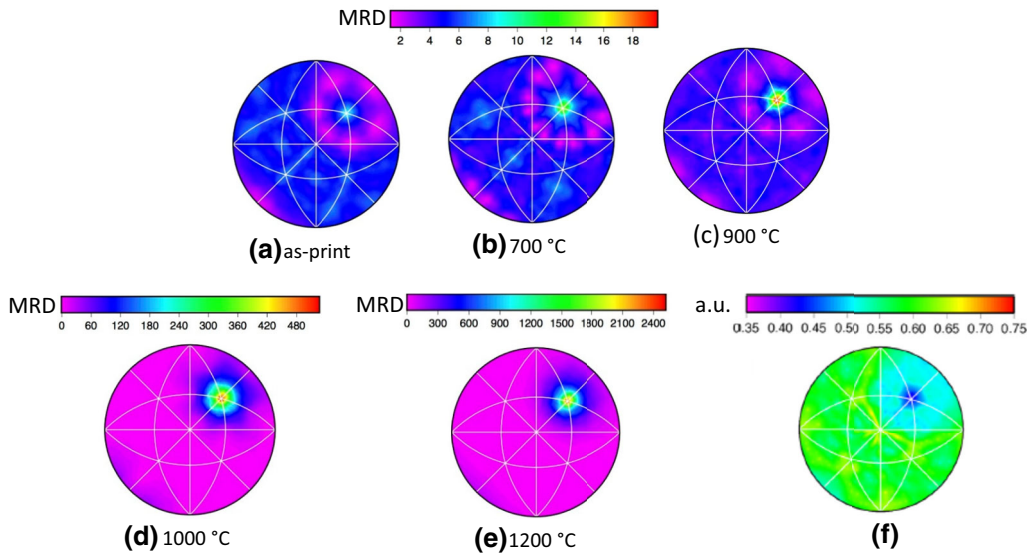


Fig. 8—(a through e) The distribution of plane normals for $\Sigma 3$ boundaries in a commercially pure Ni at different post-printing annealing treatment temperatures. (f) The distribution of grain boundary energy for $\Sigma 3$ boundaries in a commercially pure Ni, reprinted with permission from Ref. 35. MRD and a.u. represents multiples of a random distribution and arbitrary unit, respectively.

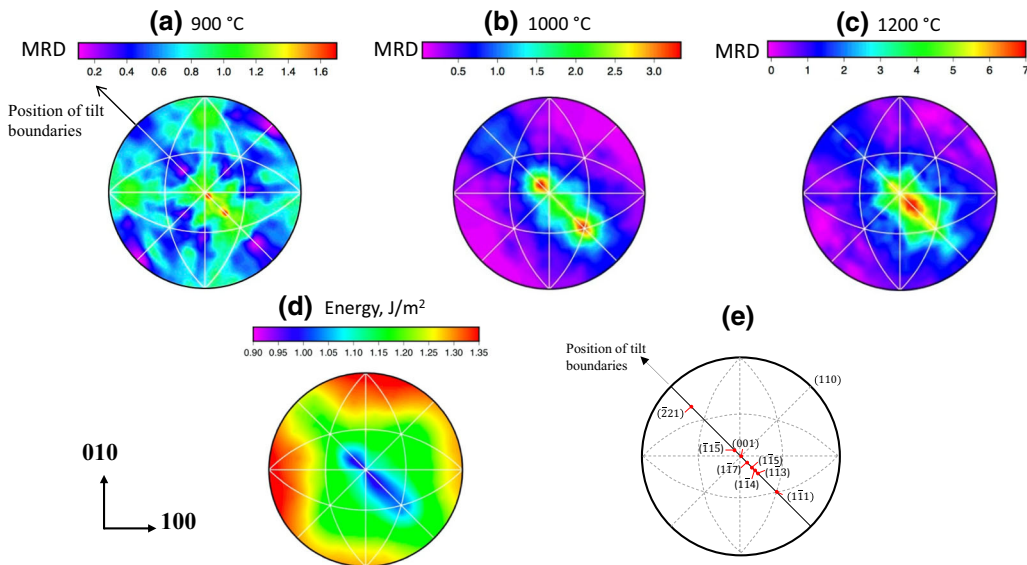


Fig. 9—(a through c) The distribution of plane normals for $\Sigma 9$ boundaries in a commercially pure Ni at different post-printing annealing treatment temperatures. (d) The distribution of grain boundary energy for $\Sigma 9$ boundaries in pure Ni, plotted with permission from the data presented in Ref. 42. (e) schematic representation of [110] tilt boundary plane positions. MRD represents multiples of a random distribution.

the mobility of grain boundary, and ultimately restricts the multiple twinning process (*i.e.*, lowering the CSL boundaries). This is an area which requires further investigation to understand how the recrystallization process of as-built commercially pure Ni significantly enhances the $\Sigma 3$ formation in the microstructure to such an extent that it becomes comparable with the GBE Ni.

The annealing treatment also altered the grain boundary plane distribution for $\Sigma 9$ boundaries (*i.e.*, 39 deg/(101) lattice misorientation). In general, multiple peaks appeared along the zone of tilt boundary

positions, which is inversely related to the position of low energy planes for pure Ni (Figure 9). However, the annealing temperature changed the intensity and the position of the peak/s. The peak intensity progressively increased from ~ 1.7 MRD at 900 °C to ~ 7 MRD at 1200 °C (Figures 9(a) to (c)). This is largely related to the occurrence of static recrystallization in the microstructure during annealing, which enhances the population of CSL boundaries due to the twin multiplication process (*e.g.*, $\Sigma 3 + \Sigma 3 \rightarrow \Sigma 9$).^[34] Here, the population of $\Sigma 9$ boundaries increased from 0.52 ± 0.08 pct at 900 °C to 4.85 ± 0.57 pct at 1200 °C.

Two peaks appeared at the (001) and ($1\bar{1}3$) positions at 900 °C (Figures 9(a) and (e)). The distribution slightly changed at 1000 °C, displaying two peaks at the positions about ($\bar{1}1\bar{5}$) and ($1\bar{1}1$) orientations (Figures 9(b) and (e)). With an increase in the annealing temperature to 1200 °C, a single peak appeared in the distribution about ($1\bar{1}4$)/($1\bar{1}4$) symmetrical tilt position (Figures 9(c) and (e)), having the minimum energy arrangement based on the simulation (Figure 9(d)).^[42] It was recently demonstrated that the $\Sigma 9$ peak position is correlated to the characteristics of $\Sigma 3$ boundaries connected to the $\Sigma 9$ boundary at the triple junction.^[43] The impingement of fully coherent $\Sigma 3$ boundaries (*i.e.*, (111)/(111)) leads to the formation of $\Sigma 9$ boundaries with the ($1\bar{1}4$) plane orientation having the minimum energy. The deviation of $\Sigma 3$ boundaries from the ideal coherency alters the $\Sigma 9$ grain boundary plane orientation, which does not necessarily occupy the minimum energy position.

The $\Sigma 3$ boundaries with the grain boundary trace orientation within 8.66 deg deviation from the trace expected for the ideal {111} twin plane orientation were considered coherent $\Sigma 3$ boundaries in the current study. In the samples annealed below 1000 °C, most $\Sigma 3$ boundaries were incoherent (Figure 7) and the microstructure contained isolated $\Sigma 9$ boundaries (Figures 5(c) and (d)), and this leads to plane orientations different from the minimum energy ($1\bar{1}4$) orientation. By contrast, the population of coherent $\Sigma 3$ boundaries accounted for more than 50 pct of the length fraction and many of the $\Sigma 9$ boundaries in the microstructure were connected to $\Sigma 3$ boundaries (Figures 5(e), and (f) and 7). This leads to an increase in the area of boundaries with the ($1\bar{1}4$) orientation, which has the minimum energy configuration (Figures 9(c) and (d)).

The microstructural changes resulted from the post-printing annealing treatment potentially have a significant impact on the material properties, where the augment in $\Sigma 3$ population would be beneficial to fracture toughness^[19] and corrosion resistance^[20] and the texture randomisation reduces the anisotropy in the mechanical behaviour.

IV. CONCLUSIONS

In the current study, the post-printing annealing treatment of commercially pure Ni led to significant microstructural changes in terms of grain structure, grain boundary network and overall texture. At a temperature range of up to 900 °C, only small changes in the microstructure were noted. However, an approximately 10 pct increase in the grain size increased the areas of boundaries with the low energy (111) plane at the expense of higher energy boundaries with the (001) orientation. For annealing temperatures greater than 900 °C, the dominant mechanism of microstructure evolution was static recrystallization. During static recrystallization, new equiaxed grains appeared in the microstructure promoting CSL boundaries with low

energy interfaces (*i.e.*, $\Sigma 3$ and $\Sigma 9$), and ultimately leading to the randomisation of texture through the twinning multiplication process.

ACKNOWLEDGMENTS

Deakin University's Advanced Characterization Facility is acknowledged for use of the EBSD instruments.

FUNDING

Open Access funding enabled and organized by CAUL and its Member Institutions.

CONFLICT OF INTEREST

The authors declare that they have no conflict of interest.

OPEN ACCESS

This article is licensed under a Creative Commons Attribution 4.0 International License, which permits use, sharing, adaptation, distribution and reproduction in any medium or format, as long as you give appropriate credit to the original author(s) and the source, provide a link to the Creative Commons licence, and indicate if changes were made. The images or other third party material in this article are included in the article's Creative Commons licence, unless indicated otherwise in a credit line to the material. If material is not included in the article's Creative Commons licence and your intended use is not permitted by statutory regulation or exceeds the permitted use, you will need to obtain permission directly from the copyright holder. To view a copy of this licence, visit <http://creativecommons.org/licenses/by/4.0/>.

REFERENCES

1. M. Das, V.K. Balla, D. Basu, S. Bose, and A. Bandyopadhyay: *Scripta Mater.*, 2010, vol. 63, pp. 438–41.
2. B. Poorganji, E. Ott, R. Kelkar, A. Wessman, and M. Jamshidinia: *JOM*, 2020, vol. 72, pp. 561–76.
3. S. Dryepondt, P. Nandwana, P. Fernandez-Zelaia, and F. List: *Addit. Manuf.*, 2021, vol. 37, 101723.
4. S. Tekumalla, B. Selvarajou, S. Raman, S. Gao, and M. Seita: *Mater. Sci. Eng. A*, 2022, vol. 833, 142493.
5. K.M. Bertsch, G. Meric de Bellefon, B. Kuehl, and D.J. Thoma: *Acta Mater.*, 2020, vol. 199, pp. 19–33.
6. F.C. Pinto, L.S. Aota, I.R. Souza Filho, D. Raabe, and H.R.Z. Sandim: *J. Mater. Sci.*, 2022, vol. 57, pp. 9576–98.
7. T. Niendorf, S. Leuders, A. Riemer, H.A. Richard, T. Tröster, and D. Schwarze: *Metall. Mater. Trans. B*, 2013, vol. 44B, pp. 794–96.
8. O. Zinovieva, A. Zinoviev, V. Romanova, and R. Balokhonov: *Addit. Manuf.*, 2020, vol. 36, 101521.
9. H. Torbati-Sarraf, I. Ghamarian, B. Poorganji, and S.A. Torbati-Sarraf: *Electrochim. Acta*, 2020, vol. 354, 136694.
10. F. Caiazza, V. Alfieri, G. Corrado, and P. Argenio: *Int. J. Adv. Manuf. Technol.*, 2017, vol. 93, pp. 4023–31.
11. D.R. Feenstra, V. Cruz, X. Gao, A. Molotnikov, and N. Birbilis: *Addit. Manuf.*, 2020, vol. 34, 101205.
12. M. Ni, C. Chen, X. Wang, P. Wang, R. Li, X. Zhang, and K. Zhou: *Mater. Sci. Eng. A*, 2017, vol. 701, pp. 344–51.

13. X. Zhang, C. Li, M. Zheng, Z. Ye, X. Yang, and J. Gu: *Addit. Manuf.*, 2020, vol. 32, 101087.
14. N. Kouraytem, R.A. Chanut, D.S. Watring, T. Loveless, J. Varga, A.D. Spear, and O.T. Kingstedt: *Addit. Manuf.*, 2020, vol. 33, 101083.
15. E. Strumza, O. Yeheskel, and S. Hayun: *Addit. Manuf.*, 2019, vol. 29, 100762.
16. Y. Kok, X.P. Tan, P. Wang, M.L.S. Nai, N.H. Loh, E. Liu, and S.B. Tor: *Mater. Des.*, 2018, vol. 139, pp. 565–86.
17. H. Beladi, E. Farabi, P.D. Hodgson, M.R. Barnett, G.S. Rohrer, and D. Fabijanic: *Philos. Magn.*, 2022, vol. 102, pp. 618–33.
18. D.A. West and B.L. Adams: *Metall. Mater. Trans. A*, 1997, vol. 28A, pp. 229–36.
19. V. Randle: *Acta Mater.*, 2004, vol. 52, pp. 4067–81.
20. P. Lin, G. Palumbo, U. Erb, and K.T. Aust: *Scr. Metall. Mater.*, 1995, vol. 33, pp. 1387–92.
21. Y.M. Wang, T. Voisin, J.T. McKeown, J. Ye, N.P. Caltà, Z. Li, Z. Zeng, Y. Zhang, W. Chen, T.T. Roehling, R.T. Ott, M.K. Santala, P.J. Depond, M.J. Matthews, A.V. Hamza, and T. Zhu: *Nat. Mater.*, 2018, vol. 17, pp. 63–71.
22. C. Qiu, M.A. Kindi, A.S. Aladawi, and I. Al Hatmi: *Sci. Rep.*, 2018, vol. 8, pp. 1–6.
23. C. Galera-Rueda, X. Jin, J. Llorca, and M.T. Perez-Prado: *Scripta Mater.*, 2022, vol. 211, 114512.
24. X. Wang and K. Chou: *JOM*, 2017, vol. 69, pp. 402–08.
25. S.A. Torbati-Sarraf, S. Sbbaghianrad, and T.G. Langdon: *Adv. Eng. Mater.*, 2018, vol. 20, p. 1700703.
26. S.A. Torbati-Sarraf, S. Sbbaghianrad, and T.G. Langdon: *Lett. Mater.*, 2015, vol. 5, pp. 287–93.
27. L.S. Aota, P. Bajaj, K.D. Zilnyk, E.A. Jagle, D. Ponge, H.R.Z. Sandim, and D. Raabe: *Materialia*, 2021, vol. 20, 101236.
28. A. Ariaseto, S. Kobayashi, M. Takeyama, Y. Wang, and S. Imano: *Metall. Mater. Trans. A*, 2020, vol. 51A, pp. 973–81.
29. G.S. Rohrer, D.M. Saylor, B.E. Dasher, B.L. Adams, A.D. Rollett, and P. Wynblatt: *Z. Met.*, 2004, vol. 95, pp. 197–214.
30. D.G. Brandon: *Acta Metall.*, 1966, vol. 14, pp. 1479–84.
31. J. Akram, P. Chalavadi, D. Pal, and B. Stucker: *Addit. Manuf.*, 2018, vol. 21, pp. 255–68.
32. D.N. Lee, K.H. Kim, Y.G. Lee, and C.H. Choi: *Mater. Chem. Phys.*, 1997, vol. 47, pp. 154–58.
33. H.L. Wei, J. Mazumder, and T. DebRoy: *Sci. Rep.*, 2015, vol. 5, pp. 1–7.
34. K. Miyazawa, Y. Iwasaki, K. Ito, and Y. Ishida: *Acta Crystallogr. A*, 1996, vol. 52, pp. 787–96.
35. J. Li, S.J. Dillon, and G.S. Rohrer: *Acta Mater.*, 2009, vol. 57, pp. 4304–11.
36. H. Beladi, N.T. Nuhfer, and G.S. Rohrer: *Acta Mater.*, 2014, vol. 70, pp. 281–89.
37. H. Beladi and G.S. Rohrer: *Metall. Mater. Trans. A*, 2017, vol. 48A, pp. 2781–90.
38. V. Randle: *Acta Mater.*, 1999, vol. 47, pp. 4187–96.
39. S. Mahajan, C.S. Pande, M.A. Imam, and B.B. Rath: *Acta Mater.*, 1997, vol. 45, pp. 2633–38.
40. V. Randle, G.S. Rohrer, H.M. Miller, M. Coleman, and G.T. Owen: *Acta Mater.*, 2008, vol. 56, pp. 2363–73.
41. M. Michiuchi, H. Kokawa, Z.J. Wang, Y.S. Sato, and K. Sakai: *Acta Mater.*, 2006, vol. 54, pp. 5179–84.
42. D.L. Olmsted, S.M. Foiles, and E.A. Holm: *Acta Mater.*, 2009, vol. 57, pp. 3694–3703.
43. H. Beladi, V. Tari, and G.S. Rohrer: *Materialia*, 2022, vol. 25, 101540.

Publisher's Note Springer Nature remains neutral with regard to jurisdictional claims in published maps and institutional affiliations.